High-capacity thermochemical CO_2 dissociation using iron-poor ferrites

Electronic Supplementary Information

Shang Zhai[1,9], Jimmy Rojas[1,9], Nadia Ahlborg[2], Kipil Lim[2,3], Chung Hon Michael Cheng[4,5], Chenlu Xie[1], Michael F. Toney[3], In-Ho Jung[6], William C. Chueh[2,7,8,*], Arun Majumdar[1,7,*]

[1] Department of Mechanical Engineering, Stanford University, Stanford, CA 94305, USA

[2] Department of Materials Science and Engineering, Stanford University, Stanford, CA 94305, USA

[3] Stanford Synchrotron Radiation Lightsource, SLAC National Accelerator Laboratory, Menlo Park, CA 94025, USA

[4] Department of Physics, Harvard University, Cambridge, MA 02138, USA

[5] John A. Paulson School of Engineering and Applied Sciences, Harvard University, Cambridge, MA 02138, USA

[6] Department of Materials Science and Engineering, Seoul National University, Seoul, 08826, South Korea

[7] Precourt Institute for Energy, Stanford University, Stanford, CA 94305, USA

[8] Applied Energy Division, SLAC National Accelerator Laboratory, Menlo Park, CA 94025, USA

[9] These authors contributed equally

[*] Corresponding authors: wchueh@stanford.edu; amajumdar@stanford.edu

Method

This section is partly adapted from our previous work[1].

1. Sample Synthesis

We used sol-gel synthesis for all the ferrites $Fe_yM_{1-y}O_x$ samples. Magnesium nitrate hexahydrate (99%, Sigma-Aldrich), iron(III) nitrate nonahydrate (≥98%, Sigma-Aldrich), cobalt(II) nitrate hexahydrate (≥98%, Sigma-Aldrich) and nickel(II) nitrate hexahydrate (crystalline, Sigma-Aldrich) with stoichiometric cations were dissolved in DI water with precursors:water = 1:4 in mass. EDTA (ethylenediamine tetraacetic acid, ACS, MP Biomedicals) and citric acid (≥99.5%, Sigma-Aldrich) were added to the solution with 60% and 75% the total molar amount of metal ions, respectively. (For example, if there was 1 mole of metal nitrates in total, 0.6 mol EDTA and 0.75 mol citric acid would be added.) With 300 rpm stirring, ammonium hydroxide solution (28% - 30%, Fisher Chemical) was added until pH = 11, and a dark solution formed.

The resulting solution was stirred and heated on a hot plate at 200°C for about 5 hrs (gelation). The spin bar was removed and the temperature was increased to 400°C to dry the gel overnight, during which foaming occurred and fluffy solid residues formed. The sample was then ground into powder, transferred to an alumina boat and went through the following calcination in air: 10°C/min until 800°C and 5°C/min until 1000°C, held there for an hour, 5°C/min until 800°C and then natural cooling.

The synthesis of ZrO_2-containing Fe-poor ferrite $Fe_{0.35}Ni_{0.65}O_x$-ZrO_2 was done also with sol-gel method. After nitrates were dissolved in DI water, ZrO_2 (≥99%, Sigma-Aldrich, 5μm) powder was added into the solution and sonicated for an hour to enhance mixing. Then chelating agents were added as described above and the synthesis followed the same approach as above. The amount of ZrO_2 was measured so that its mass would be 80% of the final mixture of Fe-poor ferrite $Fe_{0.35}Ni_{0.65}O_{1.2}$ and ZrO_2, in which the oxygen content x was assumed to be approximately 1.2.

2. TGA setup

The simultaneous thermal analyzer NETZSCH STA 449 F3 Jupiter was used for thermochemical

CO_2 dissociation measurement under atmospheric pressure. The system schematic is shown in **Fig. S2**. The CO sensor (Alphasense Carbon Monoxide Smart EC Sensor, Model CO-AF, CO2Meter.com) was calibrated using a gas mixture of ultra-high purity (UHP) Ar and 1000 ppm CO balance Ar (Airgas). In this system, the uncertainty of CO sensor quantification of CO yield is estimated to be ± 0.2 mL-CO/g/hour, considering ± 3 ppm uncertainty of CO sensor. The as synthesized samples were fully oxidized, as shown in synthesis method. The integrated CO yields from TGA setup were originally recorded in mL-CO per gram of the fully oxidized samples. The CO yields derived from the CALPHAD model (see **Method** Part **6**) used the ferrite composition of the average oxygen stoichiometry between thermally reduced and CO_2 oxidized materials. Similarly, the experimental yields in mL-CO per gram of fully oxidized sample were all converted to be in mL-CO per gram of sample at average oxygen stoichiometry between thermally reduced and CO_2 oxidized states. Such conversions changed the yields by less than 6%.

A Zirox ZR5 oxygen sensor measured O_2 partial pressure at the exhaust. The background pO_2 was found to be around 10 ppm (5 to 20 ppm) when UHP Ar or CO_2+Ar mixture was purged. This small leak was found to originate from the TGA and gas lines.

Thermogravimetry (TG) time-history data can be used to quantify O_2 evolutions. A "blank" experiment with no sample preceded each measurement, to identify the portion of mass change associated with temperature and gas environment change; meanwhile the CO sensor confirms background CO concentration. The sample mass is about 0.13 g for each test. The mass increase during the CO_2-splitting half-cycle could be theoretically assigned to incorporation of oxygen from CO_2 into the sample and converted into CO yield (mL-CO per gram of oxide). However, one should consider the possible contribution to sample mass increase from accidental sample oxidation by background O_2 rather than CO_2, even in the presence of CO background partial pressure[1]. To validate our data, we have compared the CO yield derived from TG, with the yield from CO profile integration of the measurement made by the CO sensor. We found them to agree within error bar (**Fig. S11**). In this paper, the presented CO yields are derived from CO sensor measurement unless otherwise noted.

Before each experiment, 150 sccm UHP Argon (Ar) was used to purge the system for about 1 hour until pO_2 stabilized to about 10 ppm. Then at 40°C/min ramp rate, the TGA furnace reached

1100°C; for T_H = 1300°C, a 20°C/min ramp rate was used for further heating due to TGA equipment requirement. At T_H, thermal reduction went on before it was cooled down at 50°C/min to T_L. Then CO_2 and CO (balance Ar) were mixed and injected to produce different ratios of $CO:CO_2$ partial pressures and CO_2 splitting reaction was studied.

3. Quenching

CTF 17/300 CARBOLITE tube furnace was used as a reactor for quenching. Sol-gel synthesized samples were ground with mortar and pestle into powder and went through thermal reduction and/or CO_2 splitting step(s) and finally quenched under Ar immediately. X-ray characterizations were done on such quenched samples. For a thermal reduction quench, for instance, 100 sccm ultra-high purity Ar was purged into the tube furnace at room temperature until the pO_2 sensor showed ~20 ppm. The furnace was then ramped up to T_H at 5°C/min, and after 3 hours, the alumina boat containing the sample was pushed from the hot zone to the (actively) cooled upstream side of the furnace in 1 second. To achieve this, the Ar flow rate was increased to 600 mL/min to avoid back-flow from the atmosphere, and then a long alumina rod was inserted into the tube through a downstream Ultra Torr fitting. This Ultra Torr fitting was previously plugged by another short alumina rod. After quenching by the long alumina rod, the short alumina rod was plugged back again. In a similar fashion, for a CO_2 splitting quenching test, the furnace would be cooled to T_L at 10°C/min after thermal reduction step and 20% CO_2 balance Ar (without CO background) would be purged for 3 hours. The same quenching process would take place afterwards.

4. CALPHAD/FactSage software

Complex chemical equilibria can be calculated using the thermodynamic software based on CALculation of PHase Diagram (CALPHAD) thermodynamic database. In the development of a CALPHAD thermodynamic database, all available and reliable phase diagrams, thermodynamic properties, and even crystal structure data are considered to obtain a set of consistent Gibbs energy functions for all phases in the system. In the present study, the FactSage software version 7.2 was employed for the oxidation and reduction calculation of oxides depending on partial pressure of oxygen[2]. The FactSage software is equipped with the assessed comprehensive thermodynamic databases of the oxide and metallic systems including Fe-Ni-O[3], Fe-Co-O[4], and Fe-Mg-O[5]

systems. Typically, all reliable experimental data are reproduced by the thermodynamic database within ± several mol % in composition, ± 25 ^{o}C in temperature and ± 0.25 $\log_{10}(pO_2$ [atm]) in oxygen partial pressure.

The two most relevant oxide solutions in the present study are spinel solution and rocksalt solution (in the FTOxid database, it is called as 'Monoxide' solution). The spinel solution contains the multicomponent solution covering Fe_3O_4, Co_3O_4, $MgFe_2O_4$, $CoFe_2O_4$, $NiFe_2O_4$, $NiCo_2O_4$, $MgCo_2O_4$, etc. In particular, the spinel solution is described using the Compound Energy Formalism considering the crystal structure of solution, $(Fe^{2+}, Fe^{3+}, Co^{2+}, Co^{3+}, Mg^{2+}, Ni^{2+})^{T}[Fe^{2+}, Fe^{3+}, Co^{2+}, Co^{3+}, Mg^{2+}, Ni^{2+}, Va]_2{}^{O}O_4$, where T and O represent the tetrahedral sites and octahedral sites in the spinel solution and Va means vacancy in octahedral sites. Rocksalt solution is formulated as the solution of FeO-$FeO_{1.5}$-MgO-CoO-NiO-etc., where $FeO_{1.5}$ is considered to describe the non-stoichiometry of wustite. The metallic phases were taken from FSStel database in FactSage.

Parameters are evaluated by optimizing the fit of the model to all the assessed information, also involving coexisting phases. After adjusting them to the available experimental data, this thermodynamic "optimization" for a specific chemical system can back calculate phase diagrams and thermodynamic properties. Thus, CALPHAD provides data that are rendered self-consistent and, therefore, based on thermodynamic principles. Additionally, extrapolations and interpolations can be made in a thermodynamically correct manner to solve discrepancies in available data. Overall, the resultant model database provides the best presently available description of the thermodynamic properties and phase equilibria.

For further information on this widely used thermodynamic modeling method, we refer the reader to a general introduction to CALPHAD: H. L. Lukas, S. G. Fries, B. Sundman,*Computational Thermodynamics: The Calphad Method*, Vol. 131, Cambridge University Press, Cambridge 2007.

5. Characterizations

X-ray diffraction

Beamline 2-1 at Stanford Synchrotron Radiation Lightsource (SSRL) was used to collect powder diffraction patterns using 17 keV x-ray radiation over a 2θ range of 6° to 62° (step size of 0.25° for 2θ). Glass capillary of 0.5 mm outer diameter was used to load the sample. We used SRM 660b LaB_6 material to calibrate the energy of the beam. Pilatus 100K detector was installed 700 mm away from sample. The height of the beam was 50 μm and the width of the beam was 200 μm. After data collection, we converted 2-dimensional image data to 1-dimensional data, 2θ versus intensity. Rietveld simulation were conducted with TOPAS.

For Rietveld refinement, spinel (AB_2O_4) and rocksalt MO phases were used to simulate quenched $Fe_{0.35}Ni_{0.65}O_x$ and $Fe_{0.35}Co_{0.65}O_x$. Fe, Co and Ni have very similar atomic scattering factors and, when mixed, they are difficult to distinguish on x-ray diffraction[6]. In refining cation distribution, the Rietveld model degree of freedom would be too large to converge to a certain structure. Considering this, to estimate phase fractions, it is sufficiently accurate to assume random distribution of cations: tetrahedral site (A) and octahedral site (B) of the spinel phase, and octahedral site (M) of the rocksalt phase are all set to have the same cation compositions as the bulk. Refining parameters include: Chebychev background, lattice parameter, zero error of 2θ, oxygen coordinate in the spinel phase, Biso of each site, oxygen occupancy.

The two-phase model for $Fe_{0.35}Ni_{0.65}O_x$ was set as the **Tables S3** and **S4** show. The model for $Fe_{0.35}Co_{0.65}O_x$ was set similarly. The refinement results are in **Table S2**. The trend of phase ratio change is that more reduced sample has less spinel phase fraction, as expected. For only $Fe_{0.35}Ni_{0.65}O_x$ quenched from 1300°C in Ar, the spinel phase showed double peaks across 2θ (**Fig. 2A**), which suggested two very similar spinel phases and was considered in refinement.

X-ray absorption near edge structure (XANES)

Fe K-edge, Co K-edge and Ni K-edge XANES were measured at beamline 2-2 at Stanford Synchrotron Radiation Lightsource (SSRL). Si(220) double crystal monochromator and transmission geometry were employed. The metal foil was put downstream of the sample to calibrate the beam energy. Powder samples were evenly spread and sealed between Kapton tapes. FeO, Fe_3O_4, Fe_2O_3, CoO, Co_3O_4, $LiCoO_2$, NiO, Ni_2O_3, $NiFe_2O_4$, and $CoFe_2O_4$ powder samples were purchased and measured as reference materials for elements concerned. The Athena software

was used for normalization, calibration and analysis.

SEM

Scanning electron microscopy (SEM) images were obtained on an FEI XL30 Sirion field-emission gun SEM at 5 kV. Energy-dispersive x-ray spectroscopy (EDS) mapping was carried out also at accelerating voltage of 5 kV. Lens astigmatism was addressed when necessary.

6. Thermodynamic equilibrium CO yield calculation

Thermochemistry data of ferrites, LSM perovskites (such as $La_{0.8}Sr_{0.2}MnO_{3-\delta}$), and CeO_2 were taken from our model and literature that used CALPHAD simulation[7,8] and experiments[9–11]. Those data contain oxygen (non)stoichiometry at various temperatures and pO_2 values, which can be used to calculate the thermodynamic equilibrium limit of CO production in TCDD through difference in equilibrium oxygen (non)stoichiometries between thermal reduction and CO_2 splitting conditions. Specifically, the equilibrium oxygen (non)stoichiometry at T_H was calculated for a pO_2 of 10^{-5} atm. This corresponds to a situation where the reactor pO_2 at the end of the oxygen release step is at this given value. Similarly, the equilibrium oxygen (non)stoichiometry was calculated at T_L for a range of $CO:CO_2$. Again, this corresponds to a situation where the reactor $CO:CO_2$ molar ratio is at this given value at the end of the CO production step.

For $CO:CO_2$ = 1:100, the equilibrium constant of reaction CO (g) +1/2O_2 (g) = CO_2 (g) is interpolated to be $10^{9.22}$ at 800°C (linear interpolation of the logarithms), giving equivalent pO_2 as $10^{-14.4}$ atm. For example, $Fe_{0.35}Ni_{0.65}O_x$ has equilibrium x = 1.104 at T_H = 1300°C and $pO_2 = 10^{-5}$ atm; it has x = 1.139 at T_L = 800°C and $pO_2 = 10^{-14.0}$ atm; for Ni-Fe-O system (only), the pO_2 for CO_2 splitting step is right next to phase boundary (**Fig. 3A**), so we used CALPHAD data at $10^{-14.0}$ atm instead of $10^{-14.4}$ atm for equilibrium yield calculation considering the uncertainty of model and experiments. To get equilibrium yield in mL-CO/g, oxygen stoichiometry x was calculated by average value between 1300°C and $pO_2 = 10^{-5}$ atm, versus 800°C and $pO_2 = 10^{-14.0}$ or $10^{-14.4}$ atm. The calculation is as below:

$$\frac{22400 mL-CO/\text{mol}*(1.139-1.104)\,\text{mol}}{[M(Fe)*0.35+M(Ni)*0.65+M(O)*(1.139+1.104)/2]\,\text{g}} = 10.4 \text{ mL-CO/g as predicted}$$

thermodynamic equilibrium yield for $Fe_{0.35}Ni_{0.65}O_x$.

Table S7 provides the results of the thermodynamic limit calculations.

We note that these calculations are somewhat different than that for a closed-system (i.e., batch reactor) typically done in literature, and reflect the fact that most experiments are carried out in an open-system (i.e., continuous flow reactor). In fact, if we record equilibrium pO_2 and CO/CO_2 ratio after thermal reduction and CO_2 splitting steps, respectively, in a batch reactor, and apply these pO_2 and CO/CO_2 to a continuous flow reactor test, then these two reactors will give the same O/(Fe+M) swing at equilibrium for a specific material (see **ESI Part 7** for details).

On the other hand, equilibrium phase mass ratios can be derived from the elemental compositions (**Fig. 3B, S13-S15**) and are shown in **Table S6**. The trend is consistent with phase ratios of quenched ferrites obtained from Rietveld refinement (**Table S2**). The quantitative difference can be explained as follows: thermal reduction has slow kinetics, so thermally reduced and quenched sample did not reach equilibrium and contained less rocksalt phase than equilibrium state should have; for CO_2 oxidized and quenched samples, they had CO_2 + Ar without CO background ($CO:CO_2 = 0$), so they would produce smaller rocksalt phase ratio than if CO background had been present, which CALPHAD model included ($CO:CO_2$ = 1:100 and 1:1000 in **Table S6**).

7. Fed-batch vs. flow-through measurement systems

Experimentalists measure CO_2-splitting performance of candidate materials MO_x using one of two reactor types: fed-batch (closed system for each reaction step) and flow-through (open system). In a fed-batch reactor, the system starts with only inert gas and oxide inside the reactor; after heating up and thermal reduction reaches equilibrium at T_H, O_2 (at "thermal reduction pO_2"), inert gas and oxide MO_{x1} coexist in the reactor. After equilibrium is achieved O_2 gets swept out by the inert gas. Then CO_2 (with inert gas) is added to the reactor vessel containing the thermally reduced oxide material, and after equilibrium is reached and gives MO_{x2}, the product CO and the leftover reactant CO_2 (at partial pressure ratio "CO/CO_2") is swept out of the reactor. The ratio of CO produced to CO_2 supplied is called conversion in this case.

In a flow-through reactor, if the same "thermal reduction pO_2" is maintained in the supply gas

during thermal reduction until equilibrium, MO_{x1} stoichiometry will be reached as well. Afterwards, if the same "CO/CO_2" ratio is maintained in the supply gas during CO_2 splitting step until equilibrium, MO_{x2} will be the final composition of the oxide. Thermodynamically, we see a strong connection between these two systems.

Fig. S19 shows an example of such a cycle for $CoFe_2O_4$. The solid curves represent the equilibrium partial pressure of oxygen as a function of oxygen content at 1300°C and 800°C. The dash lines illustrate qualitatively the thermal reduction and CO_2 splitting processes. In the two cases described above, positions of the blue square for fed-batch and flow-through reactors will be the same; positions of the red square for both reactor systems will also be the same.

8. Oxygen exchange reaction thermodynamic analysis

Meredig and Wolverton[12] proposed the following framework for visualizing thermodynamic feasibility in two-step thermochemical cycles.

Consider the thermal reduction reaction for some oxide, MO_x that can have different oxygen contents x:

$$\frac{1}{x_1 - x_2} MO_{x_1} \rightleftharpoons \frac{1}{x_1 - x_2} MO_{x_2} + \frac{1}{2} O_2$$

Where x_1 is the initial oxygen content of the oxide and $x_2 < x_1$ & $x_2 \approx x_1$is the oxygen content of some more reduced state. If the net reaction is proceeding in the forward direction, the reaction Gibbs free energy is less than zero.

$$\Delta^{rxn} G = \frac{1}{2} G_{O_2} + \frac{1}{x_1 - x_2} G_{MO_{x_2}} - \frac{1}{x_1 - x_2} G_{MO_{x_1}} < 0$$

$\Delta^{rxn} G$ = the Gibbs free energy change of the reaction under constant temperature and pressure

G_i = the Gibbs free energy per mole of species i

If the Gibbs free energy of the oxide G_{MO_x} is differentiable with respect to oxygen content x in our entire region of interest, we can make the following abbreviation:

$$g_O(x_1) = \lim_{x_2 \to x_1} \frac{G_{MO_{x_1}} - G_{MO_{x_2}}}{x_1 - x_2}$$

g_O = the partial molar Gibbs free energy of oxygen of the metal oxide

The reaction free energy is then:

$$\Delta^{rxn}G = \frac{1}{2}G_{O_2} + (-g_O) < 0$$

The Gibbs Free energy of oxygen can be further expressed as:

$$G_{O_2} = H^{\circ}_{O_2} - T_H\left[S^{\circ}_{O_2} - R\ln\frac{P_{O_2}}{P^{ref}}\right]$$

$H^{\circ}_{O_2}$ = the (standard) molar enthalpy of pure molecular oxygen gas at temperature T_H and pressure P^{ref} (1 atm in this analysis)

$S^{\circ}_{O_2}$ = the (standard) molar entropy of pure molecular oxygen gas at temperature T_H and pressure P^{ref}

The reaction free energy is now:

$$\Delta^{rxn}G = \frac{1}{2}\left(H^{\circ}_{O_2} - T_H\left[S^{\circ}_{O_2} - R\ln\frac{P_{O_2}}{P^{ref}}\right]\right) + (-g_O) < 0$$

Moving the terms for the gas to the opposite side of the inequality gives

$$(-g_O) < -\frac{1}{2}\left(H^{\circ}_{O_2} - T_H\left[S^{\circ}_{O_2} - R\ln\frac{P_{O_2}}{P^{ref}}\right]\right)$$

The partial molar free energy of the oxide can be expressed in terms of partial molar enthalpy and entropy:

$$(-h_O) - T_H(-s_O) < -\frac{1}{2}\left(H^{\circ}_{O_2} - T_H\left[S^{\circ}_{O_2} - R\ln\frac{P_{O_2}}{P^{ref}}\right]\right)$$

Moving all terms to the right hand side except $(-h_O)$ gives an equation with the form of a line of $(-h_O)$ vs $(-s_O)$

$$(-h_O) < T_H(-s_O) - \frac{1}{2}\left(H^{\circ}_{O_2} - T_H\left[S^{\circ}_{O_2} - R\ln\frac{P_{O_2}}{P^{ref}}\right]\right) \qquad [1]$$

It can be seen that $(-h_O)$ and $(-s_O)$ are properties of the metal oxide, and an active material with properties below the line formed by expression [1] will thermally reduce at temperature T_H and P_{O_2} until the oxygen content y (and P_{O_2} for a closed system) reach values such that the equality holds.

An equivalent analysis for the carbon dioxide splitting reaction gives a second equation:

$$\frac{1}{x_1 - x_2}MO_{x_2} + CO_2 \rightleftharpoons \frac{1}{x_1 - x_2}MO_{x_1} + CO$$

$$(-h_O) - T_L(-s_O) > -\left(H^{\circ}_{CO_2} - H^{\circ}_{CO} - T_L\left[S^{\circ}_{CO_2} - S^{\circ}_{CO} - R\ln\frac{P_{CO_2}}{P_{CO}}\right]\right)$$

H°_i = the standard molar enthalpy of pure gas species i at temperature T_L and pressure P^{ref}

S_i° = the standard molar enthalpy of pure gas species i at temperature T_L and pressure P^{ref}

$\frac{P_{CO_2}}{P_{CO}}$ = the ratio of partial pressure of carbon dioxide to carbon monoxide

Moving all terms except $(-h_O)$ to the right gives

$$(-h_O) > T_L(-s_O) - \left(H_{CO_2}^\circ - H_{CO}^\circ\right) + T_L\left[S_{CO_2}^\circ - S_{CO}^\circ - R\ln\frac{P_{CO_2}}{P_{CO}}\right] \quad [2]$$

A material with properties above the line formed by expression [2] will be oxidized by CO_2 and produce CO until oxygen content y (and ratio $\frac{P_{CO_2}}{P_{CO}}$ for a closed system) reach values such that the equality holds.

Inequalities [1] and [2] can be plotted in $(-h_O)$ vs $(-s_O)$ space to map out a (infinite) triangular shape area of thermodynamic properties for which a single oxide can perform both thermal reduction and carbon dioxide splitting.

If a material has known series of h_O and s_O it can be represented on this "triangle plot" as a series of dots/symbols for various y values. The h_O and s_O of the ferrite materials were extracted from the CALPHAD results as follows. Consider the analysis from the previous section describing an oxide in equilibrium with the gas phase:

$$(-h_O) - T(-s_O) = -\frac{1}{2}\left(H_{O_2}^\circ - T\left[S_{O_2}^\circ - R\ln\frac{P_{O_2}}{P^{ref}}\right]\right) \quad [3]$$

For each oxygen content y and temperature T in the simulation, CALPHAD returns the partial pressure of oxygen for which equilibrium is achieved between the solid and gas phases. Dividing

Equation [3] by RT and rearranging gives the Van't Hoff expression:

$$\frac{1}{2}\ln\frac{P_{O_2}}{P^{ref}} = \frac{h_O - \frac{1}{2}H^{\circ}_{O_2}}{RT} + \frac{-s_O + \frac{1}{2}S^{\circ}_{O_2}}{R}$$

If $h_O - \frac{1}{2}H^{\circ}_{O_2}$ and $-s_O + \frac{1}{2}S^{\circ}_{O_2}$ are assumed to be constant within the temperature range of interest, $\frac{1}{2}\ln\frac{P_{O_2}}{P^{ref}}$ will have the form of a line against 1/T with

$$\underset{vs1/T}{slope} = \frac{h_O - \frac{1}{2}H^{\circ}_{O_2}(T_{mean})}{R}$$

And

$$\underset{vs1/T}{intercept} = \frac{-s_O + \frac{1}{2}S^{\circ}_{O_2}(T_{mean})}{R}$$

Where T_{mean} in our analysis is the temperature halfway between T_H and T_L.

Supplemental Figures

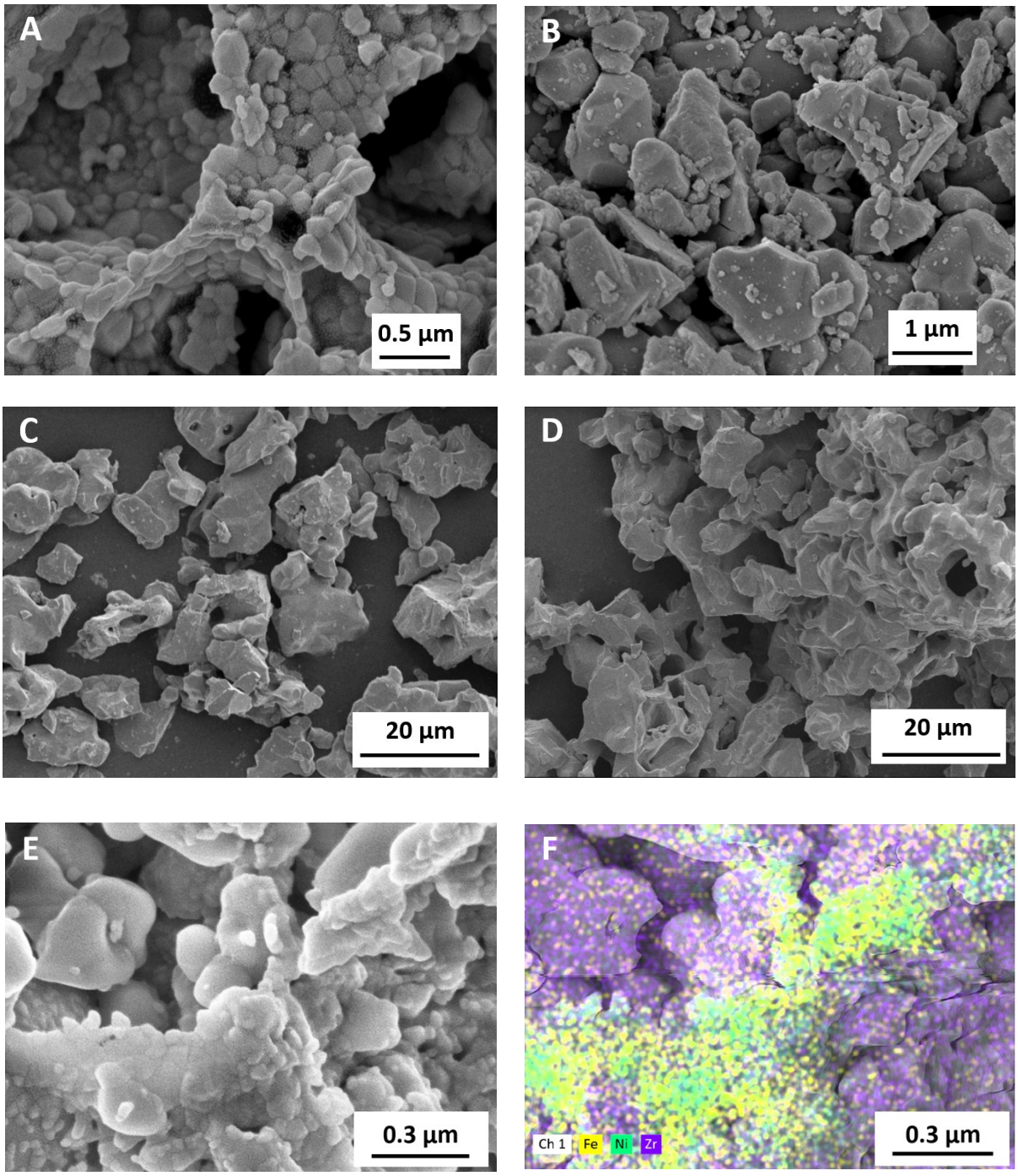

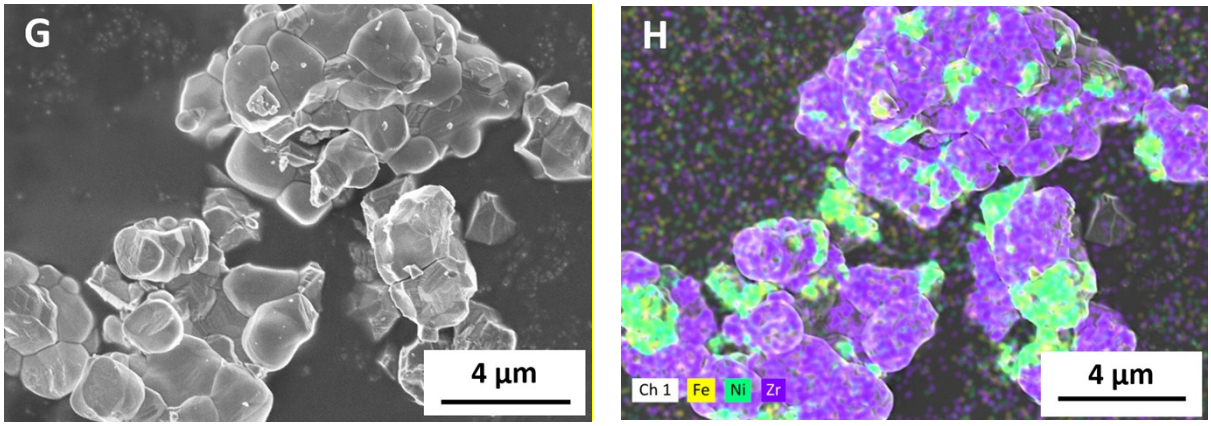

Fig. S1 | Scanning electron microscope images of Fe-poor ferrites. **A**, As-synthesized $Fe_{0.35}Ni_{0.65}O_x$. **B**, As-synthesized $Fe_{0.45}Co_{0.55}O_x$. **C**, $Fe_{0.35}Ni_{0.65}O_x$ after 10 cycles of T_H = 1300°C and T_L = 800°C. **D**, $Fe_{0.45}Co_{0.55}O_x$ after 10 cycles of T_H = 1300°C and T_L = 800°C. **E**, As-synthesized $Fe_{0.35}Ni_{0.65}O_x$-ZrO_2 (80% ZrO_2 mass fraction). **F**, Energy-dispersive x-ray spectroscopy (EDS) map of as-synthesized $Fe_{0.35}Ni_{0.65}O_x$-ZrO_2 (80% ZrO_2 mass fraction). **G**, $Fe_{0.35}Ni_{0.65}O_x$-ZrO_2 (80% ZrO_2 mass fraction) after 10 cycles of T_H = 1300°C and T_L = 800°C. **H**, Energy-dispersive x-ray spectroscopy (EDS) map of $Fe_{0.35}Ni_{0.65}O_x$-ZrO_2 (80% ZrO_2 mass fraction) after 10 cycles of T_H = 1300°C and T_L = 800°C.

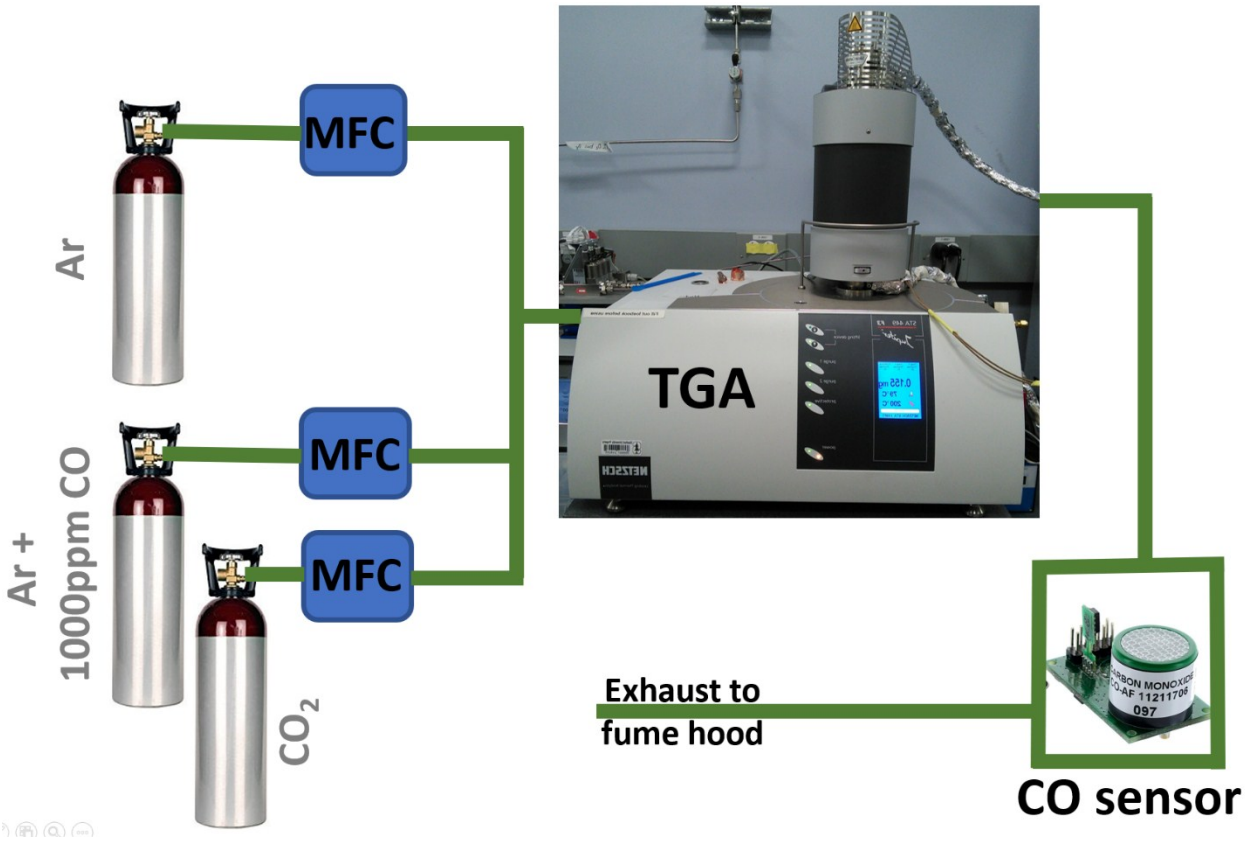

Fig. S2 | TGA-CO sensor setup.

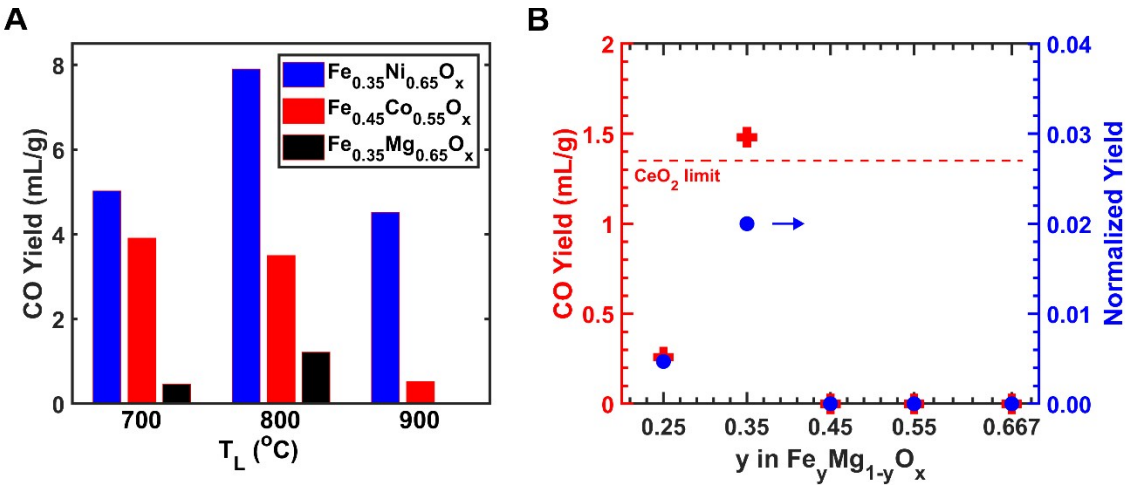

Fig. S3 | Two-step thermochemical CO_2 dissociation performance and thermodynamics of Fe-poor ferrites, related to Fig. 1. Reaction conditions are: (1) thermal reduction under T_H = 1300°C and pO_2 = 10 ppm, (2) CO_2 splitting with background gas partial pressure $CO:CO_2$=1:100. Measurements had 5 hours reaction time for both thermal reduction and CO_2 splitting. "Normalized yield" was calculated by dividing measured CO yield by "Fe redox limit" (see main text). Thermodynamic equilibrium CO yield of CeO_2 was indicated by dash line.

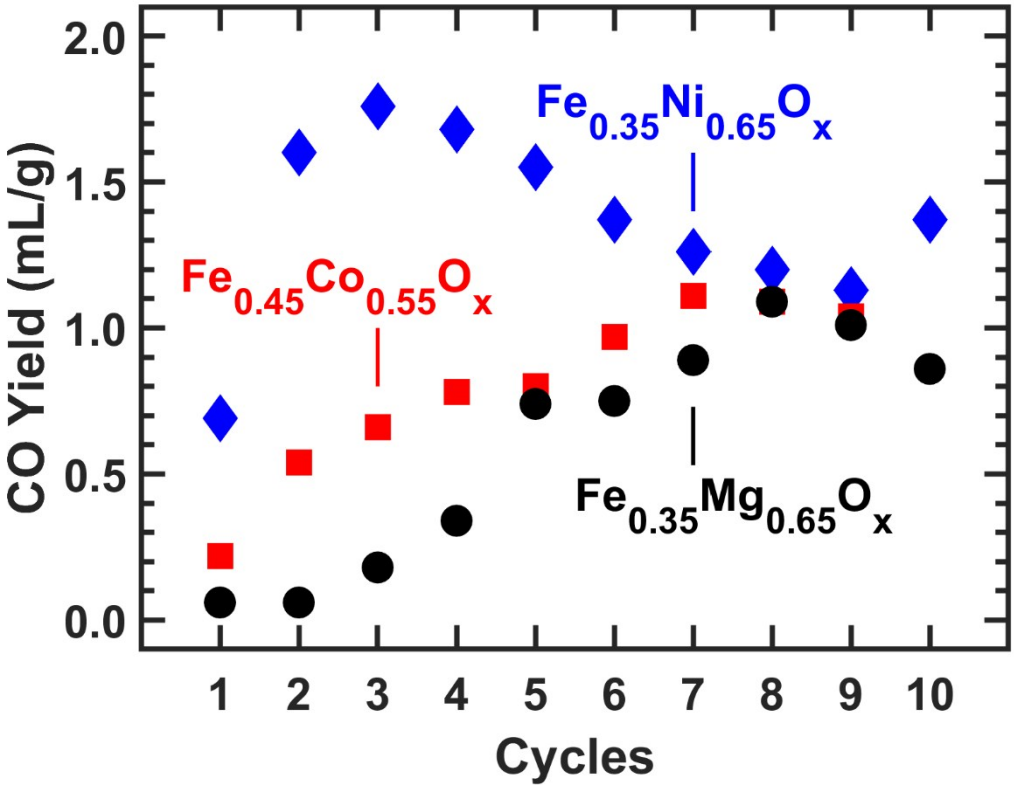

Fig. S4 | Multi-cycle thermochemical CO_2 dissociation performance, related to Fig. 1. $Fe_{0.35}Ni_{0.65}O_x$, $Fe_{0.45}Co_{0.55}O_x$ and $Fe_{0.35}Mg_{0.65}O_x$ were tested. Each cycle included 1 hour of thermal reduction plus 1 hour of CO_2 splitting. Reaction conditions were: (1) thermal reduction under T_H = 1300°C and pO_2 = 10 ppm, (2) CO_2 splitting under T_L = 800°C and background gas partial pressure $CO:CO_2$ = 1:100.

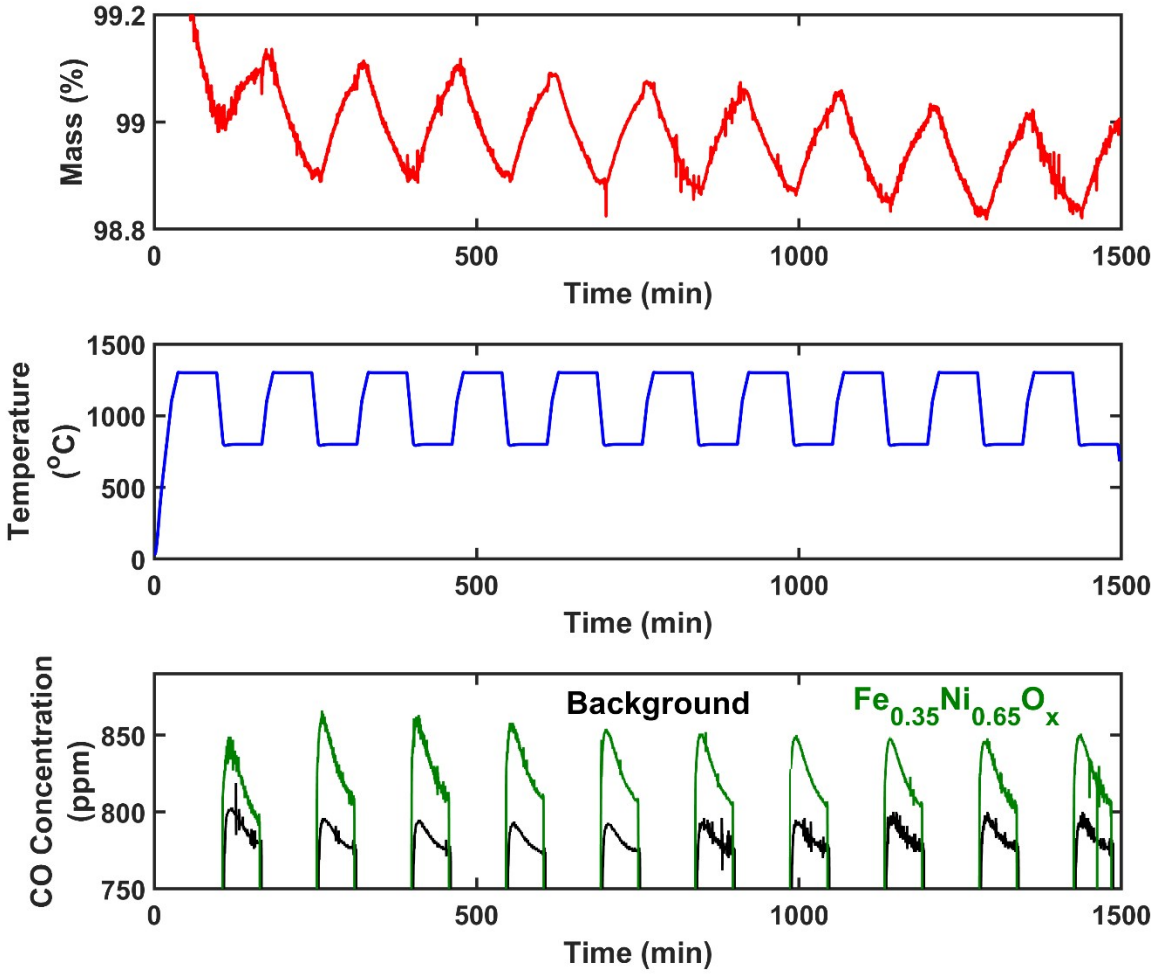

Fig. S5 | Thermogravimetry, temperature and CO concentration profiles of ten-cycle tests of two-step thermochemical CO_2 reduction using $Fe_{0.35}Ni_{0.65}O_x$, related to Fig. 1. Reaction conditions were: (1) thermal reduction under T_H = 1300°C and pO_2 = 10 ppm, (2) CO_2 splitting under T_L = 800°C and with background gas partial pressure CO:CO_2=1:100. Measurements had 1 hour reaction time for both thermal reduction and CO_2 splitting.

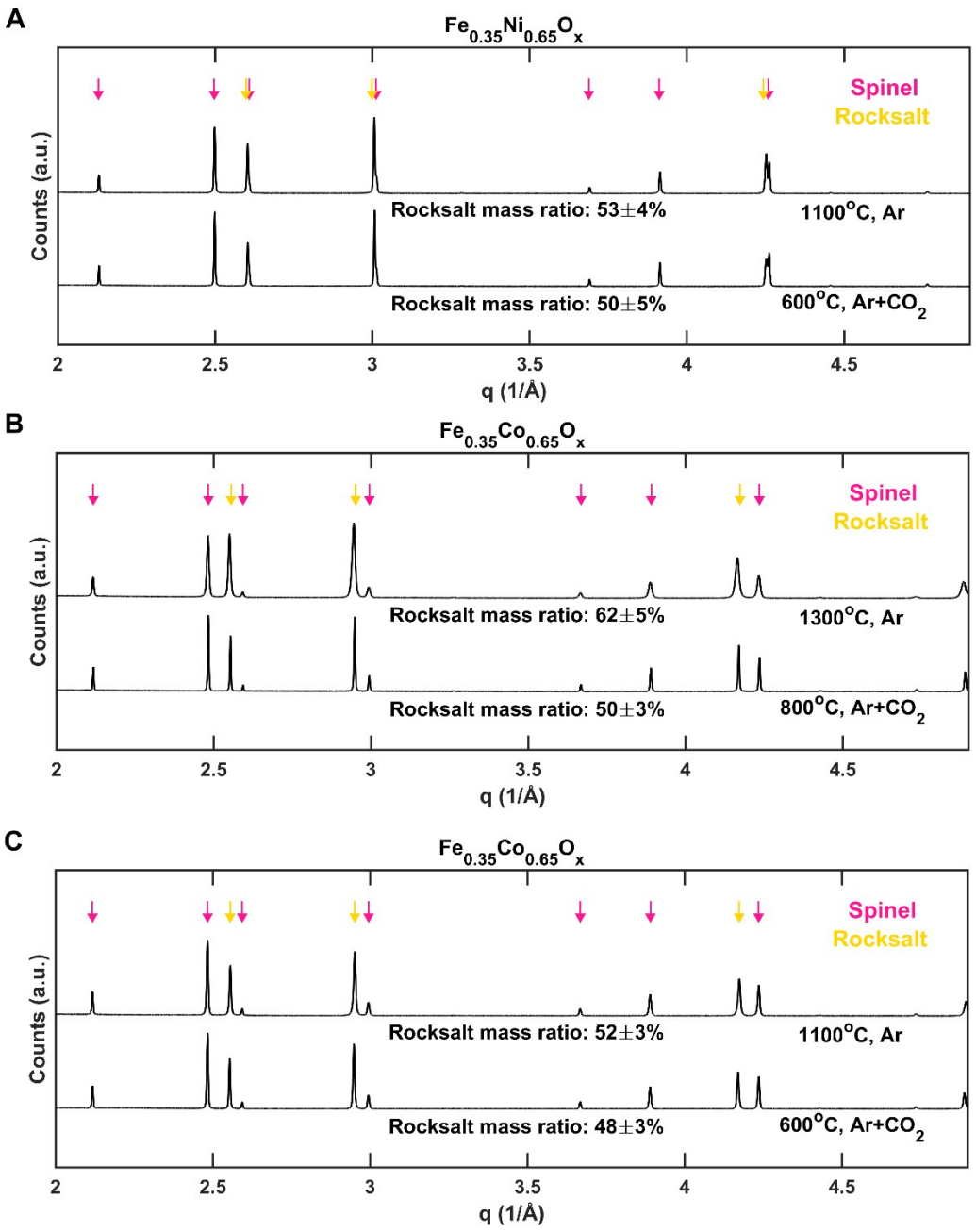

Fig. S6 | X-ray diffraction of quenched Fe-poor ferrites, related to Fig. 2. Rocksalt phase mass ratio is from Rietveld refinement.

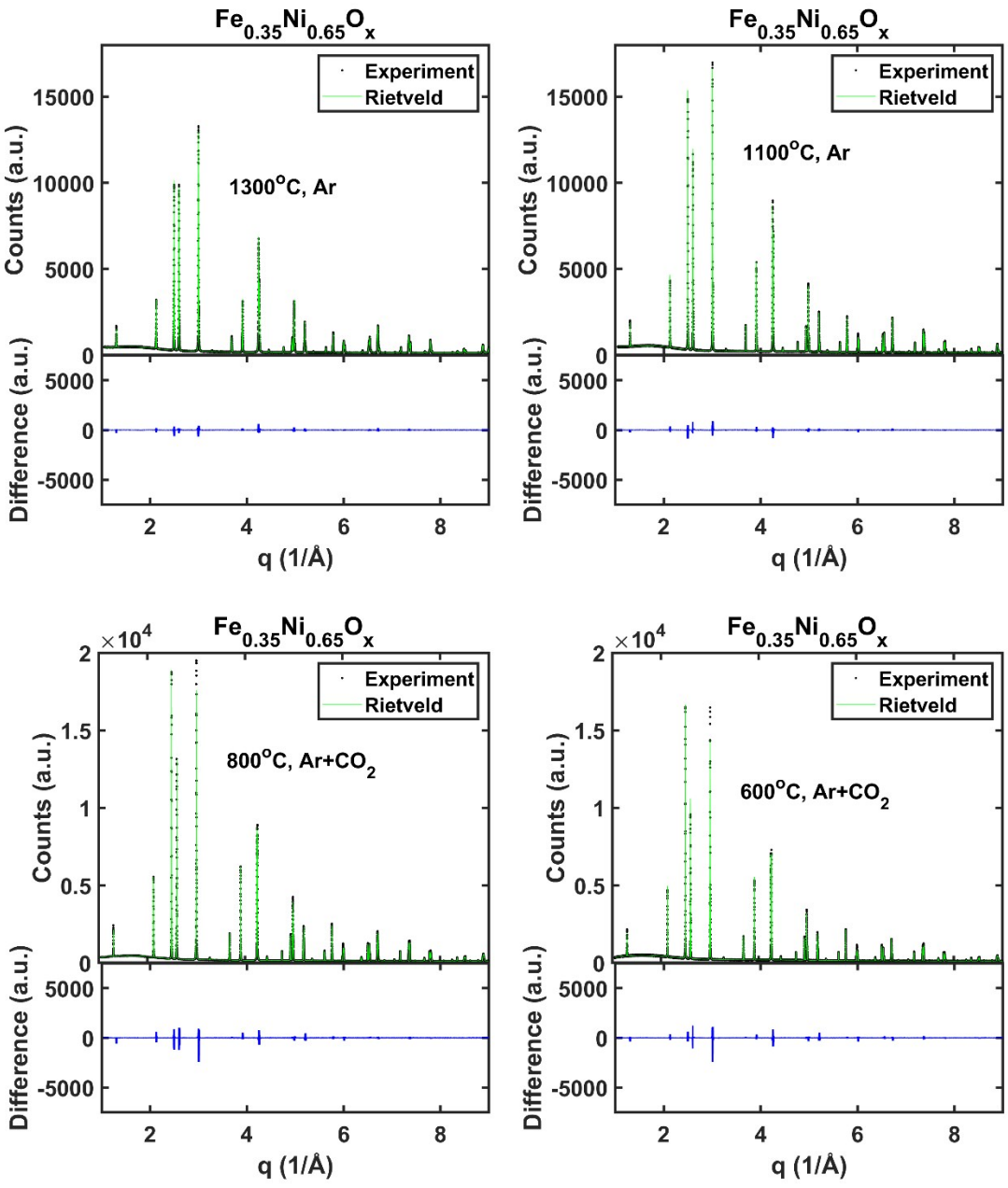

Fig. S7 | Experimental data, Rietveld refinement and difference plots of x-ray diffraction of quenched Fe-poor ferrite $Fe_{0.35}Ni_{0.65}O_x$, related to Fig. 2.

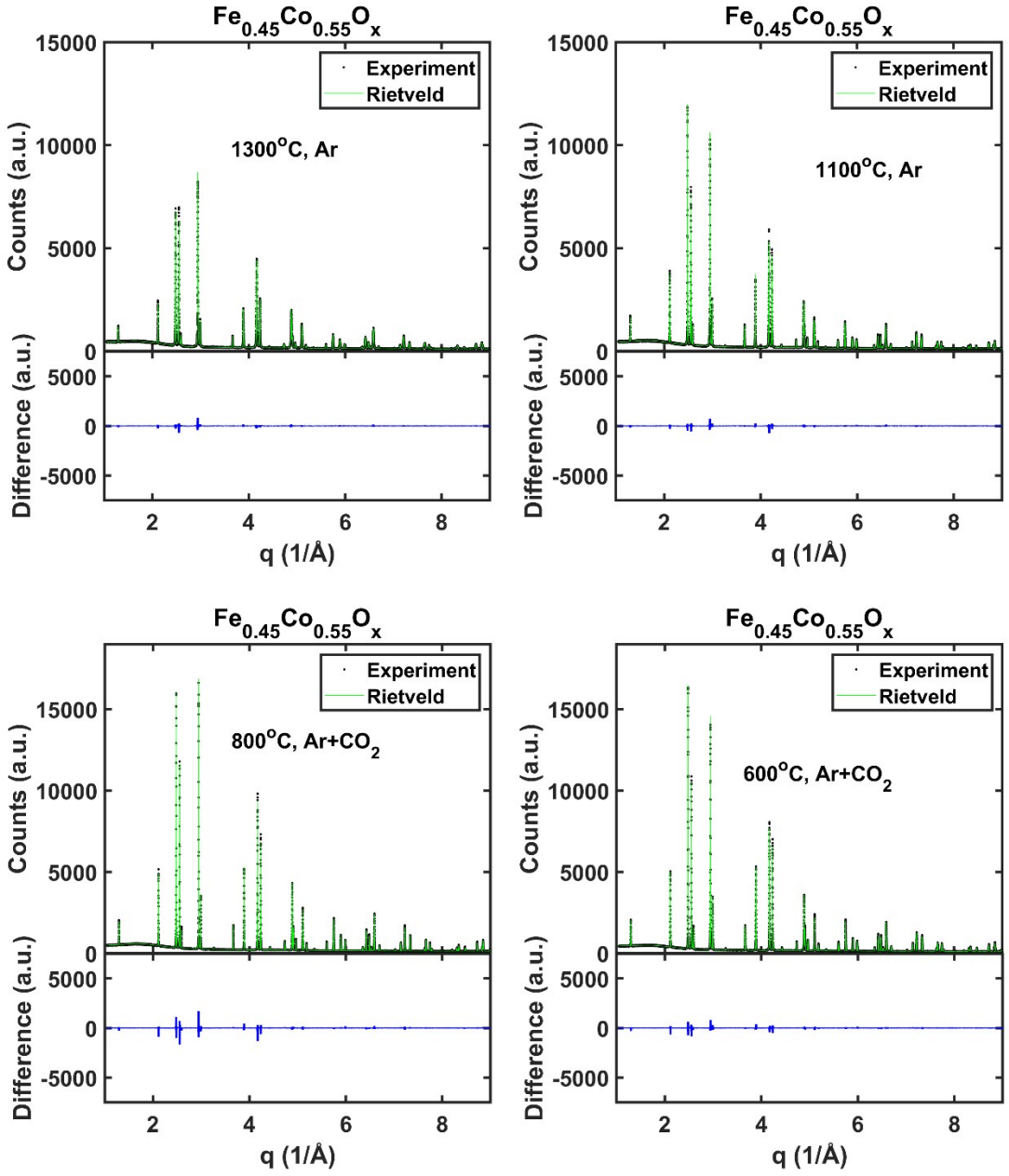

Fig. S8 | Experimental data, Rietveld refinement and difference plots of x-ray diffraction of quenched Fe-poor ferrite $Fe_{0.45}Co_{0.55}O_x$, related to Fig. 2.

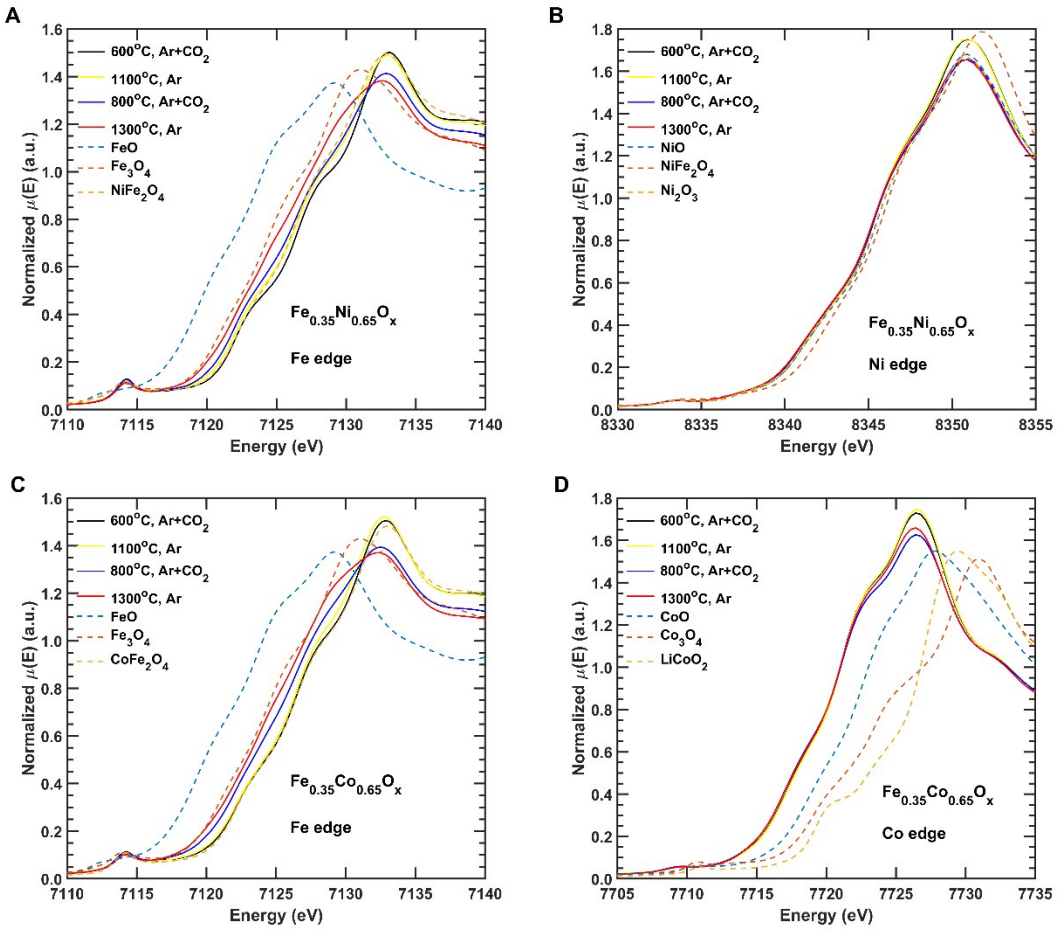

Fig. S9 | XANES of quenched Fe-poor ferrites at Fe, Co and Ni K edges, related to Fig. 2.

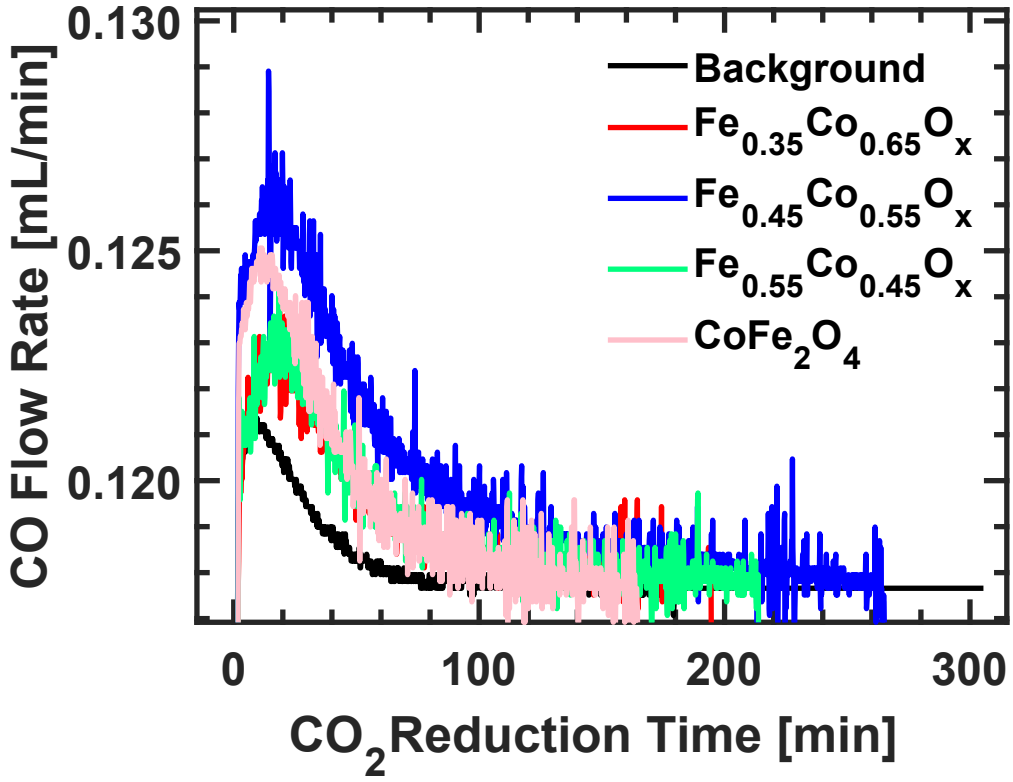

Fig. S10 | CO concentration profiles of two-step thermochemical CO_2 reduction using $Fe_yCo_{1-y}O_x$, related to Fig. 1. "Background" indicates a test of background CO concentration without sample. Reaction conditions were: (1) thermal reduction under T_H = 1300°C and pO_2 = 10 ppm, (2) CO_2 splitting under T_L = 800°C and background gas partial pressure CO:CO_2 = 1:100. Measurements had 5 hours reaction time for both thermal reduction and CO_2 splitting. Sample masses are about 0.13 g.

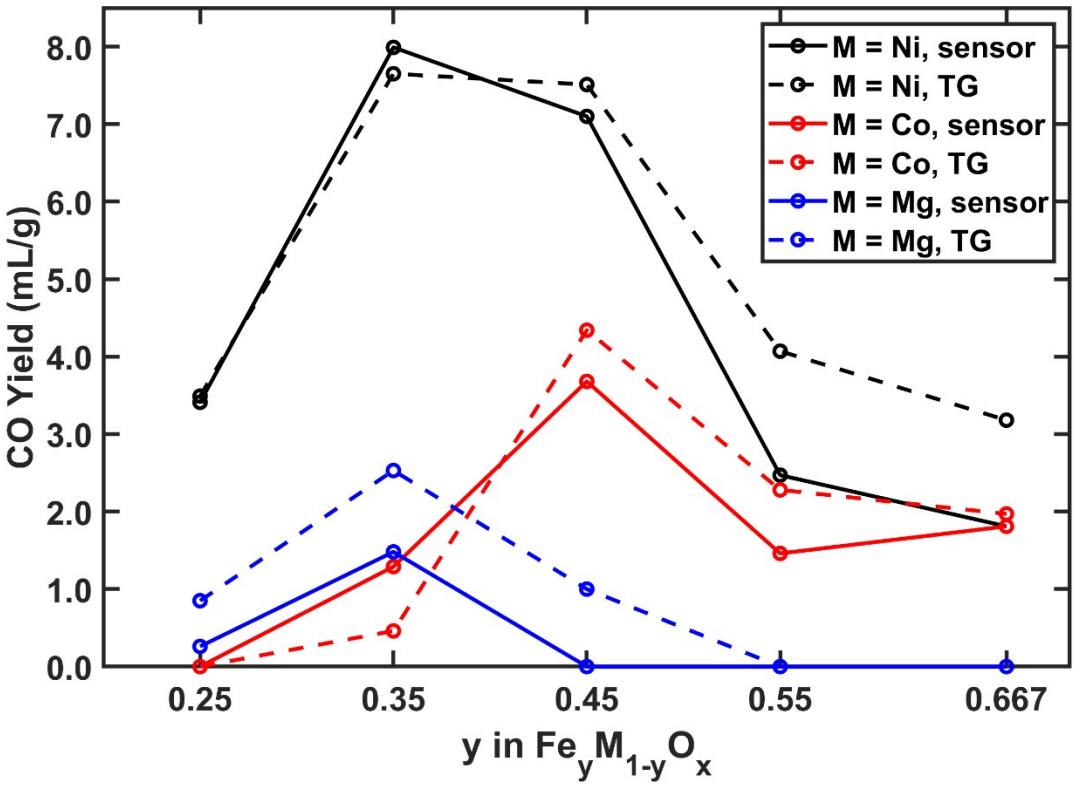

Fig. S11 | Comparison of TG derived and CO sensor measurement derived CO yield, related to Fig. 1. Error bars of CO sensor derived yield is ± 1.0 mL-CO/g. See **Method** for uncertainty analysis.

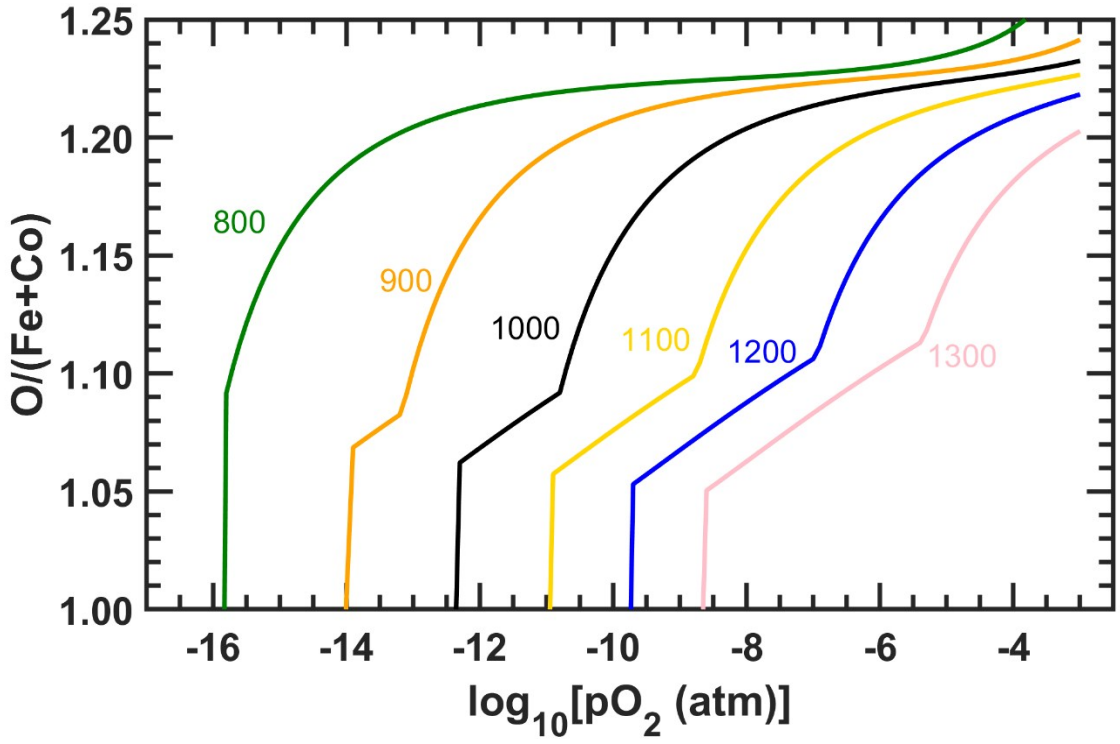

Fig. S12 | $Fe_{0.45}Co_{0.55}O_x$ oxygen stoichiometry dependence on oxygen partial pressure at various temperatures (°C) from CALPHAD, related to Fig. 3.

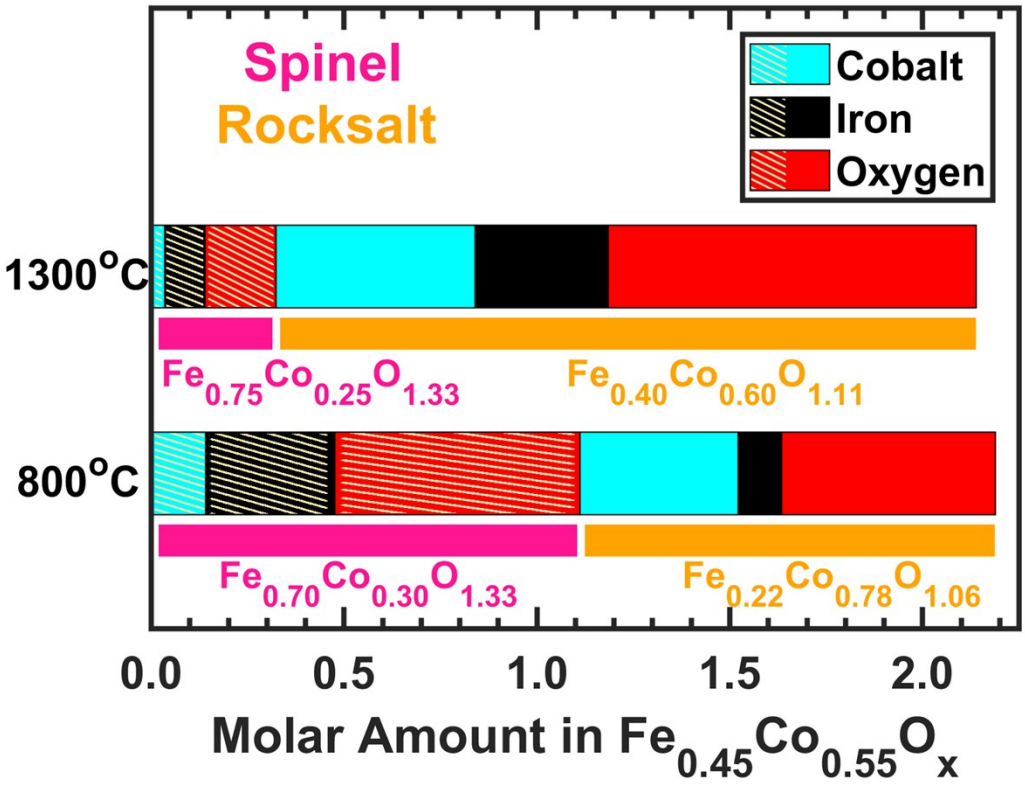

Fig. S13 | $Fe_{0.45}Co_{0.55}O_x$ elemental compositions of rocksalt and spinel phases from CALPHAD modeling, related to Fig. 3. Conditions are 1300°C and pO_2 = 10 ppm, and 800°C and $pO_2 = 10^{-14}$ atm. Molar amount of cations added up to one for each condition.

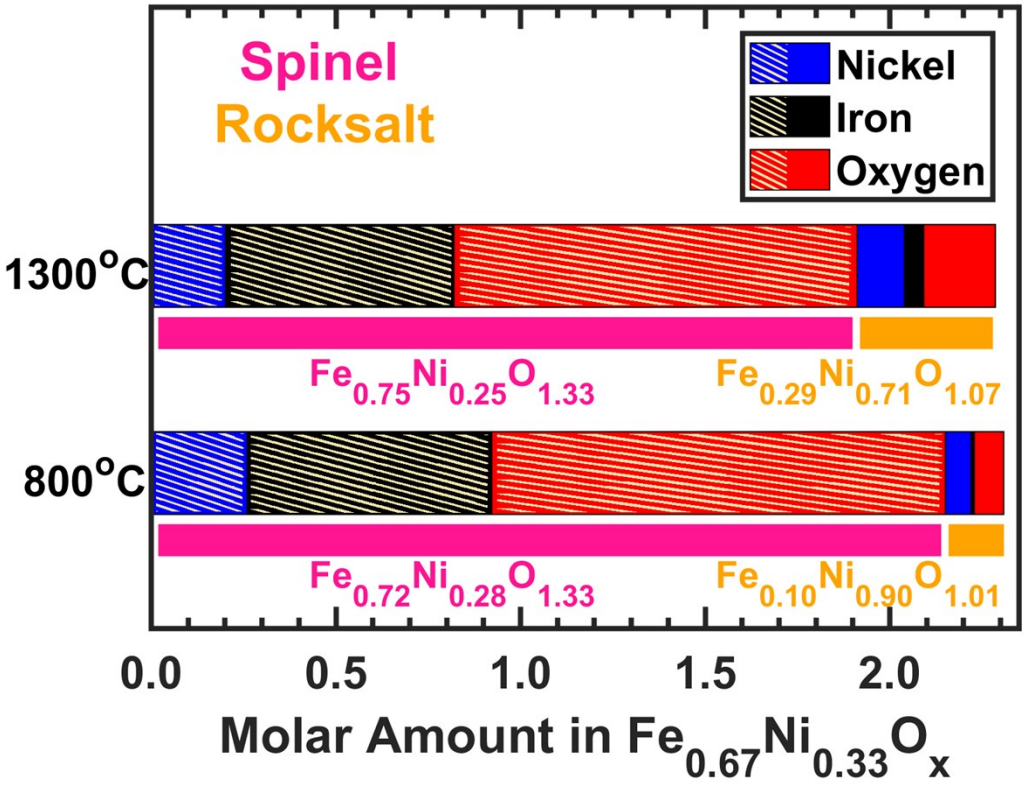

Fig. S14 | $Fe_{0.67}Ni_{0.33}O_x$ elemental compositions of rocksalt and spinel phases from CALPHAD modeling, related to Fig. 3. Conditions are 1300°C and pO_2 = 10 ppm, and 800°C and $pO_2 = 10^{-14}$ atm. Molar amount of cations added up to one for each condition.

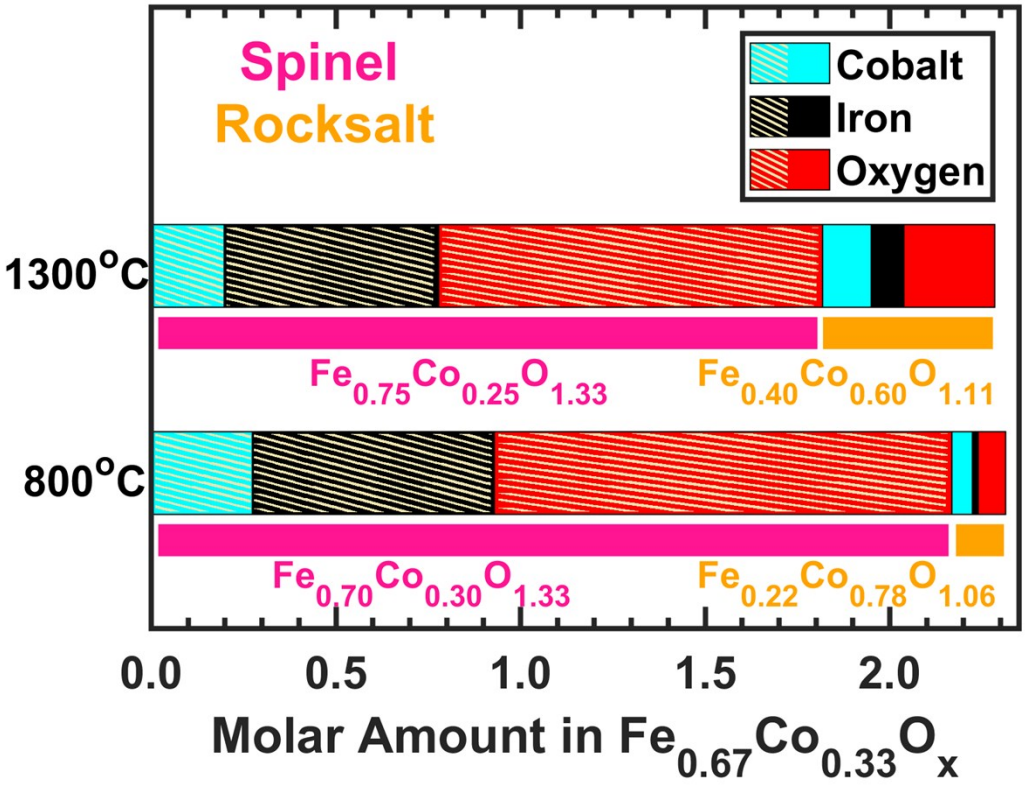

Fig. S15 | $Fe_{0.67}Co_{0.33}O_x$ elemental compositions of rocksalt and spinel phases from CALPHAD modeling, related to Fig. 3. Conditions are 1300°C and pO_2 = 10 ppm, and 800°C and $pO_2 = 10^{-14}$ atm. Molar amount of cations added up to one for each condition.

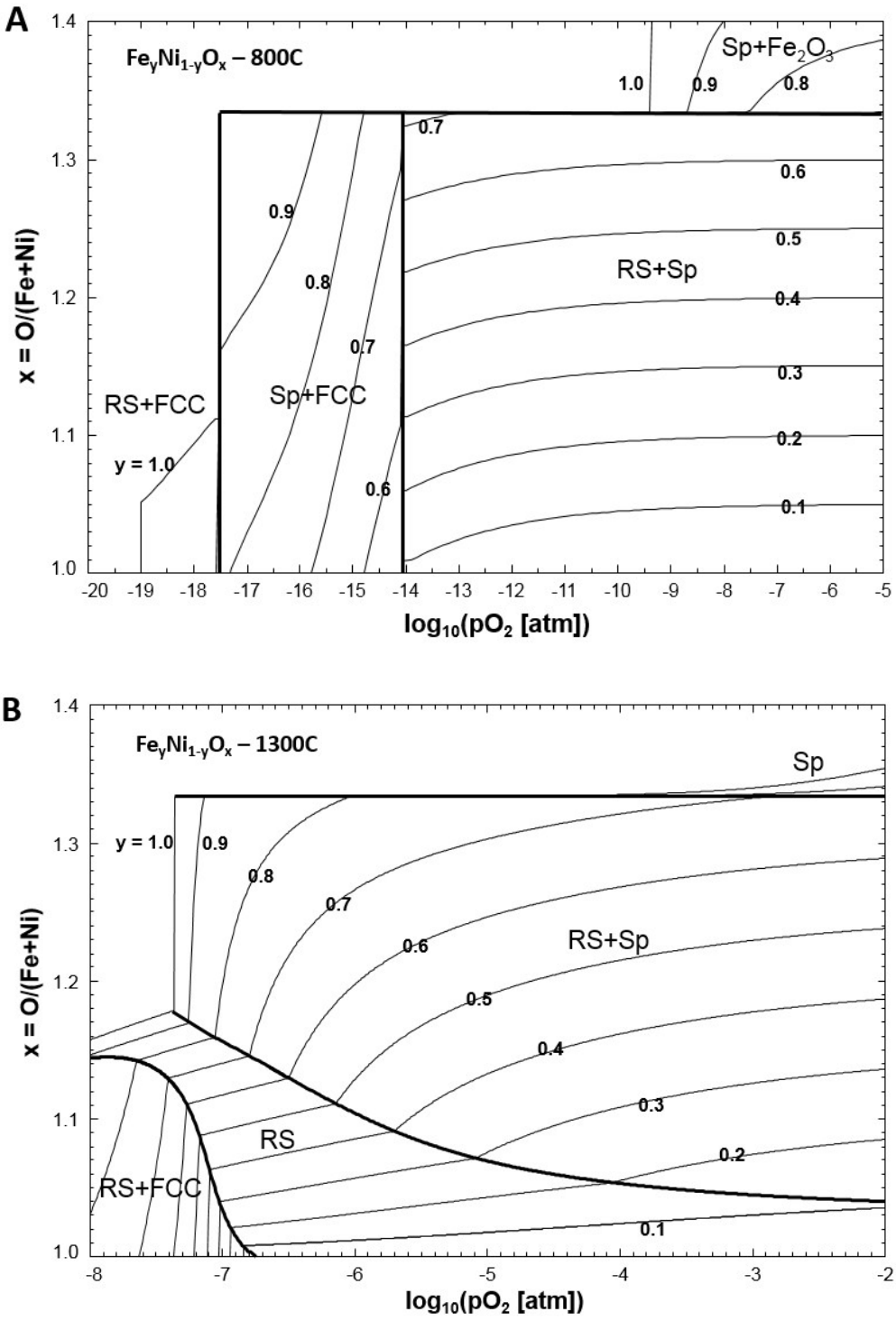

Fig. S16 | Oxygen stoichiometry dependence on $\log_{10}(pO_2\ [atm])$ for $Fe_yNi_{1-y}O_x$ system, related to Fig. 3. 800°C (**A**) and 1300°C (**B**), y is indicated on each curve. RS stands for rocksalt phase; Sp stands for spinel phase; FCC stands for a metallic phase.

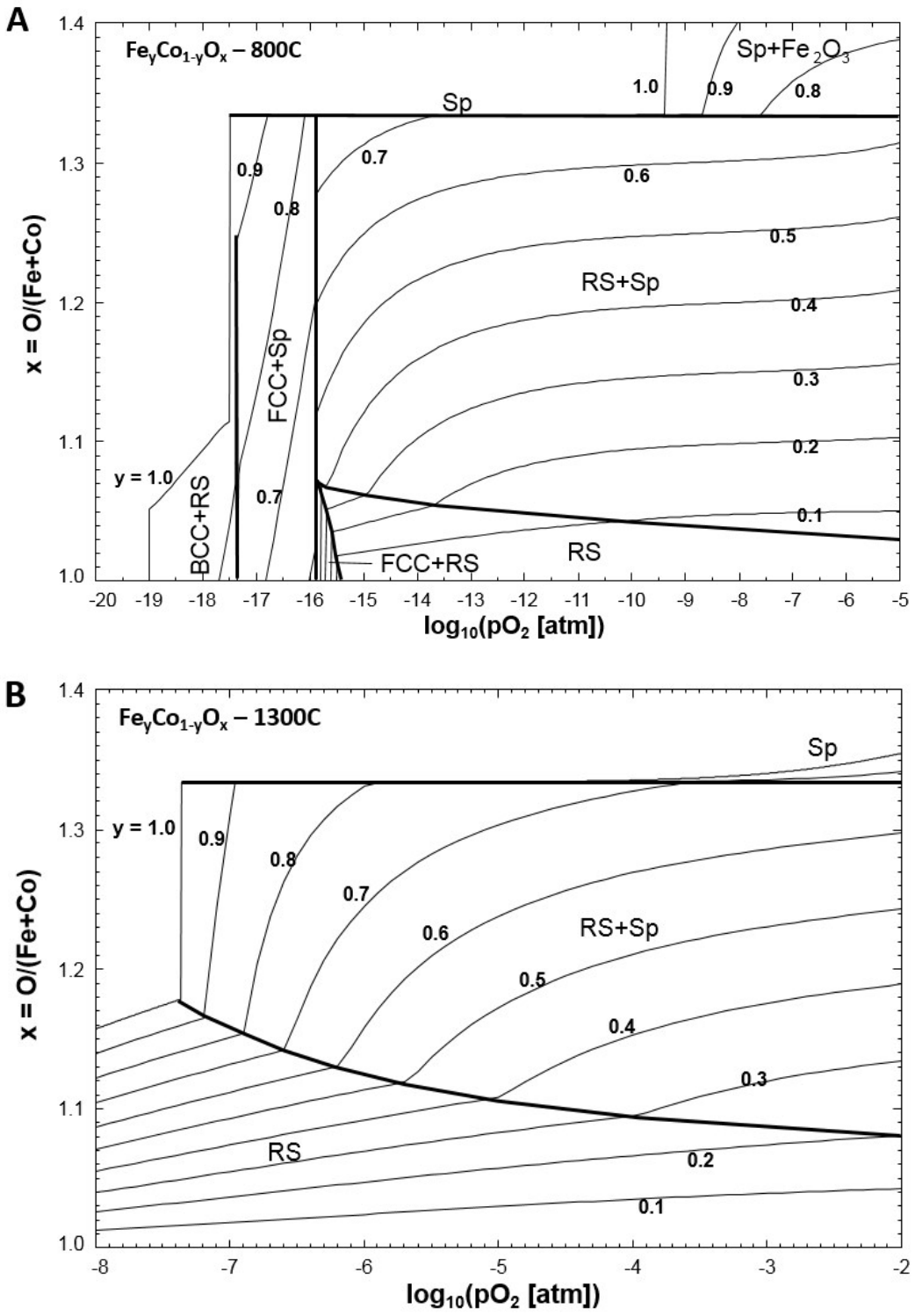

Fig. S17 | Oxygen stoichiometry dependence on $\log_{10}(pO_2\ [atm])$ for $Fe_yCo_{1-y}O_x$ system, related to Fig. 3. 800°C (**A**) and 1300°C (**B**), y is indicated on each curve. RS stands for rocksalt phase; Sp stands for spinel phase; FCC stands for a metallic phase; BCC stands for another metallic phase.

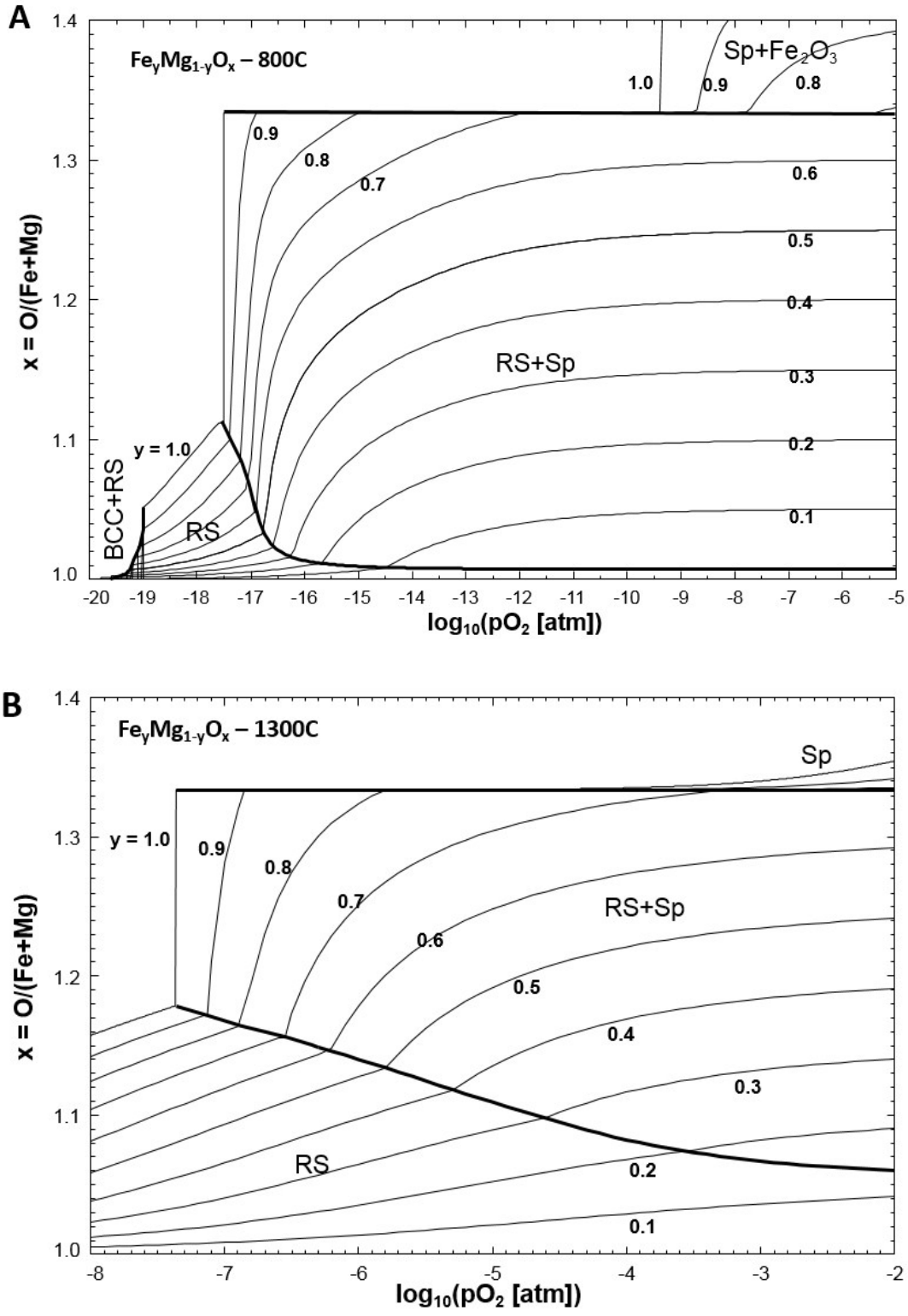

Fig. S18 | Oxygen stoichiometry dependence on $\log_{10}(pO_2$ [atm]) for $Fe_yMg_{1-y}O_x$ system, related to Fig. 3. 800°C (**A**) and 1300°C (**B**), y is indicated on each curve. RS stands for rocksalt phase; Sp stands for spinel phase; BCC stands for a metallic phase.

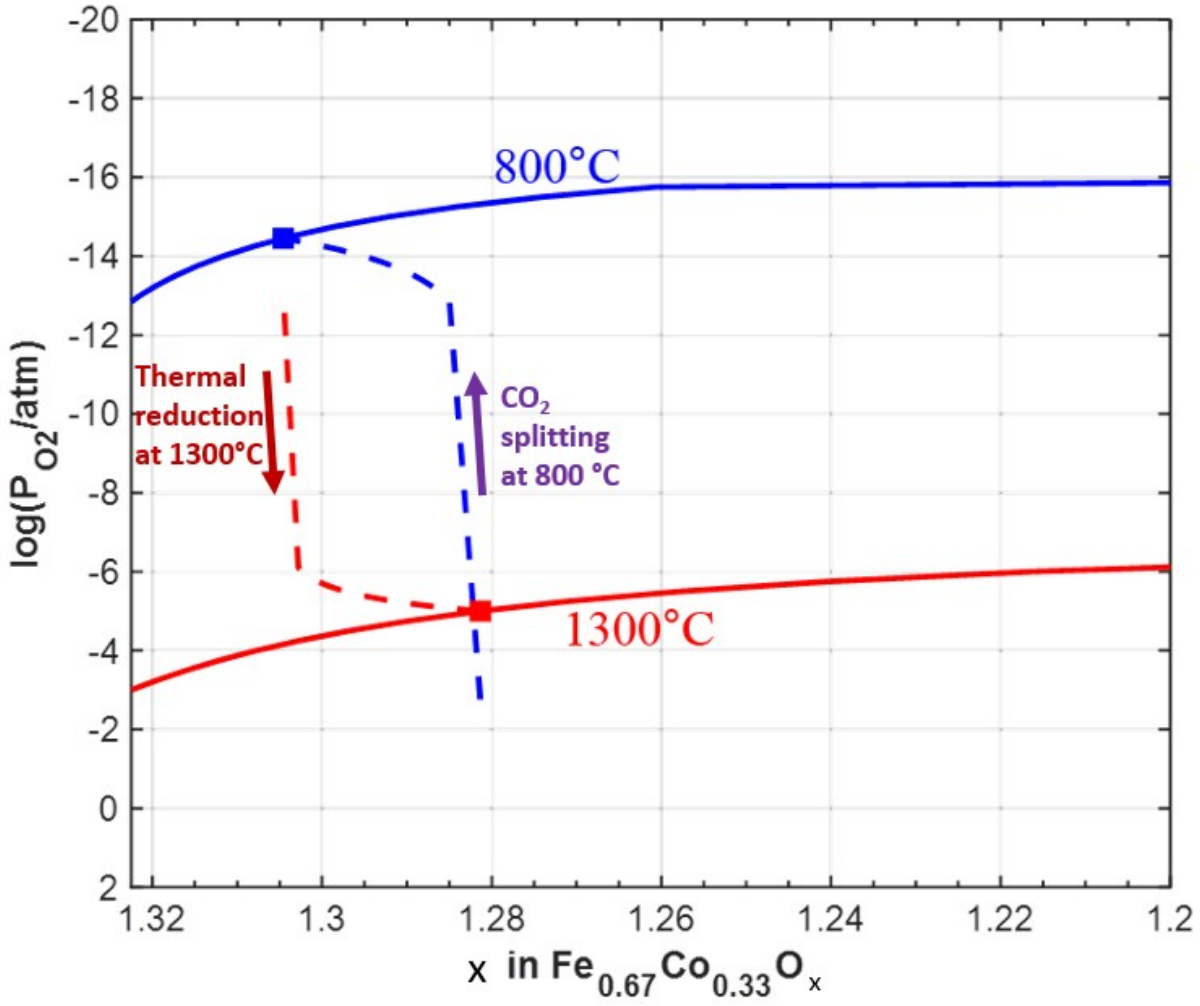

Fig. S19 | Two-step cycle schematic on the plot of oxygen stoichiometry vs. $\log_{10}(pO_2$ [atm]) for $Fe_{0.67}Co_{0.33}O_x$. The dash lines are illustratively showing the two reaction steps but not indicating specific reaction route.

Supplemental Tables

Table S1. "Fe redox limit" CO yield [mL/g] , related to Fig. 1. Assuming Fe, Mg, Co and Ni are at +3, +2, +2 and +2 when calculating formula weight, to get reaction-condition-independent CO yield limits.

y	x	$Fe_yNi_{1-y}O_x$	$Fe_yCo_{1-y}O_x$	$Fe_yMg_{1-y}O_x$
0.25	1.125	36.9	36.8	55.8
0.35	1.175	51.2	51.1	72.4
0.45	1.225	65.4	65.3	86.7
0.55	1.275	79.5	79.3	99.3
0.667	1.3335	95.6	95.5	112.0

Table S2. Rietveld refinement phase ratios of quenched Fe-poor ferrites, related to Fig. 2

Sample	Sweep gas	T_{quench} [°C]	Rocksalt Phase		Spinel Phase	
			Mass Ratio [%]	Lattice param. [Å]	Mass Ratio[%]	Lattice param. [Å]
$Fe_{0.35}Ni_{0.65}O_x$	CO_2+Ar	600	50(5)	4.18(2)	50(5)	8.3386(2)
		800	53(2)	4.18(1)	47(2)	8.34509(9)
	Ar	1100	53(4)	4.18(1)	47(4)	8.337(2)
		1300	61(3)	4.18764(2)	28(2)	8.34(6)
					11(5)	8.36(4)
$Fe_{0.35}Co_{0.65}O_x$	CO_2+Ar	600	48(3)	4.261(9)	52(3)	8.39(1)
		800	50(3)	4.261(6)	50(3)	8.390(6)
	Ar	1100	52(3)	4.257(8)	48(3)	8.39(1)
		1300	62(5)	4.27(1)	38(5)	8.39(3)

Table S3. Spinel phase (space group: Fd-3m) settings for $Fe_{0.35}Ni_{0.65}O_x$, related to Fig. 2.

Atom	Wyckoff positions	x	y	z	Occupancy
Fe1	8b	0.375	0.375	0.375	0.35
Ni1					0.65
Fe2	16c	0	0	0	0.35
Ni2					0.65
O1	32e	t	t	t	refined

The value of t varies slightly from sample to sample.

Table S4. Rocksalt phase (space group: Fm-3m) settings for $Fe_{0.35}Ni_{0.65}O_x$, related to Fig. 2.

Space group: Fm-3m					
Atom	**Wyckoff positions**	**x**	**y**	**z**	**Occupancy**
Fe3	4a	0	0	0	0.35
Ni3					0.65
O1	4b	0.5	0.5	0.5	refined

Table S5. CALPHAD predicted equilibrium elemental molar compositions of Fe-poor ferrites $Fe_yM_{1-y}O_x$, related to Fig. 3

Material	$log_{10}(pO_2$ [atm])	$CO:CO_2$	T [°C]	Rocksalt Phase Fe/(Fe+M)	Rocksalt Phase O/(Fe+M)	Spinel Phase Fe/(Fe+M)	Spinel Phase O/(Fe+M)
$Fe_{0.35}Ni_{0.65}O_x$	-14.0	1:100	800	0.104	1.009	0.718	1.333
	-12.4	1:1000		0.055	1.008	0.691	1.333
	-5.0	-	1300	0.288	1.069	0.754	1.333
$Fe_{0.67}Ni_{0.33}O_x$ ($NiFe_2O_4$)	-14.0	1:100	800	The same as $Fe_{0.35}Ni_{0.65}O_x$			
	-12.4	1:1000					
	-5.0	-	1300				
$Fe_{0.45}Co_{0.55}O_x$ ($CoFe_2O_4$)	-14.0	1:100	800	0.218	1.055	0.705	1.333
	-12.4	1:1000		0.143	1.048	0.682	1.333
	-5.0	-	1300	0.402	1.108	0.746	1.333
$Fe_{0.67}Co_{0.33}O_x$ ($CoFe_2O_4$)	-14.0	1:100	800	The same as $Fe_{0.45}Co_{0.55}O_x$			
	-12.4	1:1000					
	-5.0	-	1300				

Table S6. CALPHAD predicted equilibrium rocksalt mass ratios of Fe-poor ferrites, related to Fig. 3.

Material	$log_{10}(pO_2$ [atm])	$CO:CO_2$	T [°C]	Rocksalt Phase Mass Ratio [%]
$Fe_{0.35}Ni_{0.65}O_x$	-14.0	1:100	800	59
	-12.4	1:1000		53
	-5.0	-	1300	86
$Fe_{0.45}Co_{0.55}O_x$	-14.0	1:100	800	51
	-12.4	1:1000		42
	-5.0	-	1300	86
$Fe_{0.35}Co_{0.65}O_x$	-14.0	1:100	800	72
	-12.4	1:1000		61
	-5.0	-	1300	100

Table S7. Thermodynamic equilibrium CO yield from CALPHAD, related to Fig. 3.

Material	T_H [°C]	T_L [°C]	$CO:CO_2$ during CO_2 splitting	Equilibrium CO yield [mL/g]
$Fe_{0.35}Ni_{0.65}O_x$	1300	800	1:100	10.4
			1:1000	16.1
$Fe_{0.45}Co_{0.55}O_x$			1:100	11.2
			1:1000	20.6
$Fe_{0.35}Mg_{0.65}O_x$			1:100	9.4
			1:1000	15.1

Supplemental References

1 S. Zhai, J. Rojas, N. Ahlborg, K. Lim, M. F. Toney, H. Jin, W. C. Chueh and A. Majumdar, *Energy Environ. Sci.*, 2018, **11**, 2172–2178.

2 C. W. Bale, E. Bélisle, P. Chartrand, S. A. Decterov, G. Eriksson, A. E. Gheribi, K. Hack, I.-H. Jung, Y.-B. Kang, J. Melançon, A. D. Pelton, S. Petersen, C. Robelin, J. Sangster, P. Spencer and M.-A. Van Ende, *Calphad*, 2016, **54**, 35–53.

3 M. A. Rhamdhani, P. C. Hayes and E. Jak, *Metall. Mater. Trans. B Process Metall. Mater. Process. Sci.*, 2008, **39**, 690–701.

4 I. H. Jung, S. A. Decterov, A. D. Pelton, H. M. Kim and Y. B. Kang, *Acta Mater.*, 2004, **52**, 507–519.

5 I. H. Jung, S. A. Decterov and A. D. Pelton, *J. Phys. Chem. Solids*, 2004, **65**, 1683–1695.

6 D. Carta, M. F. Casula, A. Falqui, D. Loche, G. Mountjoy, C. Sangregorio and A. Corrias, *J. Phys. Chem. C*, 2009, **113**, 8606–8615.

7 A. H. Bork, E. Povoden-Karadeniz and J. L. M. Rupp, *Adv. Energy Mater.*, 2017, **7**, 1601086.

8 M. Zinkevich, D. Djurovic and F. Aldinger, *Solid State Ionics*, 2006, **177**, 989–1001.

9 R. J. Panlener, R. N. Blumenthal and J. E. Garnier, *J. Phys. Chem. Solids*, 1975, **36**, 1213–1222.

10 H. Tagawa, in *Proceedings of the 5th International Symposium on Solid Oxide Fuel Cells (SOFC-V)*, Aachen, Germany, 1997.

11 J. R. Scheffe, D. Weibel and A. Steinfeld, *Energy & Fuels*, 2013, **27**, 4250–4257.

12 B. Meredig and C. Wolverton, *Phys. Rev. B - Condens. Matter Mater. Phys.*, 2009, **80**, 1–8.